Chaotic scattering on a billiard

Vincent J. Daniels, Michel Vallières, and Jian Min Yuan
Department of Physics and Atmospheric Science, Drexel University, Philadelphia, Pennsylvania 19104-9984
(Received 26 June 1997)

We investigate chaotic scattering on an attractive step potential with a quadrupolar deformation. The phase space features of the bound billiard are studied by using the notion of symmetry lines to find periodic orbits. We show that the scattering dynamics is intimately linked to structures in the bound billiard (infinite potential wall) phase space. The existence of preferred scattering directions is shown to be a consequence of large scale features of the phase space such as the period-two orbits. Self-similarity in the scattering functions is directly linked to unstable periodic orbits of the bound phase space. The main observations and methodology are applicable to concave billiards in general. [S1063-651X(98)02002-9]

PACS number(s): 05.45.+b, 03.65.Nk

I. INTRODUCTION

The study of chaos in billiards has a long and productive history. Some of the earliest work with billiard systems dates back to Bunimovich and his proof that the stadium billiard is ergodic [1,2]. Also early on Berry showed that various deformations of circular billiards exhibited regular, chaotic, or mixed behavior [3]. Volumes have been written on various kinds of closed billiard geometries [4–9] as well as billiards with holes in the wall [10,11] to study scattering problems. However, little work has been done to study attractive potential scattering with billiard geometries. This particular type of scattering finds applications in any physical system that is well described by a discontinuous interface with a nonspherical geometry such as deformed quantum dots, nuclei, fiber optics, and semiconductor devices. In this paper we discuss the scattering on a quadrupolar deformation of a circle. We find that the scattering functions have strongly preferred directions that persist for a wide range of deformation. A similar effect is observed by Nöckel and Stone [12] in light scattering in an optical fiber with a quadrupole cross section. We show that this behavior is directly linked to the large scale structure of the phase space, which does not change dramatically as a function of the deformation. The details of the chaotic scattering are related to the presence of unstable orbits near the critical angle for escape.

We will begin by describing the model system in the context of a deformed nucleus and introducing the phase space mapping in Sec. II. In Sec. III we will examine the bound phase space, in particular, we will use the symmetry lines of the map to determine the symmetric periodic orbits. The existence of homoclinic orbits and thus the chaotic nature of the bound billiard system is shown. In Sec. IV we apply the knowledge of the bound phase space dynamics to the study of the scattering dynamics using some specific cases to illustrate general relationships. In Sec. V we discuss the implications of the connections described in the paper and the generality of the observations.

II. MODEL SYSTEM

The model is inspired by the simplest nuclear potential shape, that is, a simple step potential in two dimensions. We introduce an angle-dependent deformation described by a radial shape function, $r_s(\theta)$. We are interested in $r_s(\theta)$, which forms a closed curve in configuration space. A shape function typically used to describe small nuclear deformations can be written

$$r_s(\theta)=[1+bP_2(\sin(\theta))], \tag{1}$$

where $P_2(x)$ is the second Legendre polynomial, all lengths are scaled by the average nuclear radius r_0, and b is the deformation parameter. This shape function remains reasonable for describing nuclei as long as $|b|<2/7$. Beyond this the shape becomes ''peanutlike,'' that is, the boundary becomes partly convex. For $b=0$ we have the circular (undeformed) nuclear step potential. We will focus on deformations around the middle of this range, $b\approx 0.15$. This shape defines the location of the step so the potential is just a product of the well depth and the step function,

$$V(r,\theta)=-V_0 S(-[r-r_s(\theta)]), \tag{2}$$

where $S(t)$ is the unit step function defined by

$$S(t)=\begin{cases}0, & t<0\\ 1, & t>0.\end{cases} \tag{3}$$

Figure 1 shows a plot of the resulting potential for $b=0.15$ and $V_0=1.0$.

The Hamiltonian in polar coordinates is

$$H=\frac{p_r^2}{2}+\frac{p_\theta^2}{2r^2}-S(-[r-r_s(\theta)])=\epsilon, \tag{4}$$

where ϵ is the scaled energy, $\epsilon\equiv E/V_0$, and V_0 is the potential depth. The potential is a constant within the domain defined by $r_s(\theta)$; if the total energy is negative, the kinetic energy is also a constant and the total energy can be scaled away.

The traditional billiard problem is a bound problem with negative total energy with no possibility of escape. We generalize this problem to a scattering situation by sending particles with positive total energy from outside the well. The trajectories followed by these particles may penetrate the

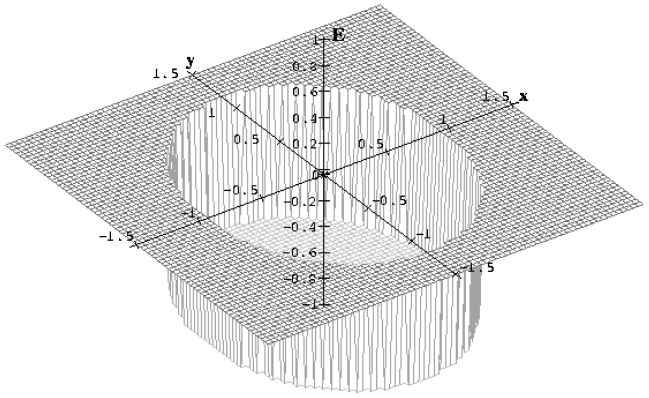

FIG. 1. A plot of the potential energy surface given by Eq. (2) with $b=0.15$ and $V_0=1.0$. All lengths and energies are in dimensionless units in this and subsequent figures.

well region, get temporarily trapped, and eventually escape. For this positive total energy case, the total energy cannot be scaled away. The kinetic energy changes as the particle crosses the shape boundary; the dynamics at the boundary will depend on the ratio of the kinetic energy on either side preventing energy scaling.

We now look briefly at the equations of motion; this is instructive yet not strictly necessary since we will be developing a map for the system. In polar coordinates they are

$$\dot{r}=p_r, \tag{5}$$

$$\dot{\theta}=\frac{p_\theta}{r^2}, \tag{6}$$

$$\dot{p}_r=\frac{p_\theta^2}{r^3}-\delta(r-r_s(\theta)), \tag{7}$$

$$\dot{p}_\theta=\frac{\partial r_s}{\partial\theta}\,\delta(r-r_s(\theta)). \tag{8}$$

It is clear from the equations of motion that when $r-r_s(\theta)\neq 0$ the motion is integrable. In the event of an intersection with the wall, $r-r_s(\theta)=0$, both the radial and angular momentum change. Zeroes of $\partial r_s/\partial\theta$ mark angles for which there is no change in angular momentum.

Map

The dynamics can be rephrased in terms of a mapping. This follows from the fact that a particle will be deflected only when it is at the step and undeflected otherwise since the potential is constant. This map will relate the coordinates in phase space from intersection to intersection with the billiard wall, the trajectory between collisions being straight lines in configuration space.

There are many different representations for two-dimensional maps. We will primarily use a map space (θ,γ) where θ is the angle at which a trajectory intersects the shape function. The second coordinate, γ, is the angle between the forward (counterclockwise) tangent to $r_s(\theta)$ at the intersection and the incoming momentum vector. The forward tangent is defined by $\vec{T}\equiv d\vec{r}_s(\theta)/d\theta$. Other sets of coordinates that we will use when convenient are (s,p) and (θ,p), where s is the arc length measured from $\theta=-\pi$ and $p=\cos(\gamma)$ is the momentum tangential to the shape at an intersection. The resulting map in (θ,p) has the form

$$\theta_{n+1}=f(\theta_n,p_n),$$

$$p_{n+1}=g(\theta_n,p_n), \tag{9}$$

which we write in terms of the nonlinear map operator, **M**,

$$\begin{pmatrix}\theta_{n+1}\\ p_{n+1}\end{pmatrix}=\mathbf{M}\begin{pmatrix}\theta_n\\ p_n\end{pmatrix}. \tag{10}$$

The algorithm for obtaining the map has two steps:

(i) Given the slope, $m(\theta_n,p_n)$, and intercept, $B(\theta_n,p_n)$, defining the line along which the particle moves after the nth intersection with the wall, find the intersection of this line with the shape function, $r_s(\theta)$. This provides θ_{n+1}.

(ii) Transform the momentum vector $\vec{p}(\theta_n,p_n)$ after the nth intersection into the new coordinate system defined at θ_{n+1}. This provides γ_{n+1} and therefore p_{n+1}.

The first step is the nonlinear part of the map. Generally, this step involves the solution of

$$r_s(\theta_{n+1})\sin(\theta_{n+1})=m(\theta_n,p_n)r_s(\theta_{n+1})\cos(\theta_{n+1})+B(\theta_n,p_n). \tag{11}$$

For $r_s(\theta)$ given by Eq. (1) this is a transcendental equation and so must be solved numerically. The second step involves a coordinate system rotation and finding the new momentum direction. The latter depends on whether the particle is transmitted or reflected at the wall.

Consider a trajectory with momentum $\vec{p}_0$ before an intersection and $\vec{p}_1$ after. We decompose these vectors into components parallel and perpendicular to the tangent at the intersection. From the definition of the potential we see that the force will always be perpendicular to the shape and pointing to the inside. Thus the parallel component of momentum is conserved so that

$$p_0\cos(\gamma_0)=p_1\cos(\gamma_1), \tag{12}$$

where p_0 and p_1 are the magnitudes of the momenta and are constant everywhere within a given region and

$$p_i=\sqrt{2\{E-V[r-r_s(\theta)]\}}.$$

Equation (12) is precisely Snell's law from geometric optics with the refractive indices being p_0 and p_1 and the angles measure with respect to the tangent rather than the normal. The behavior of a trajectory intersecting the shape function is analogous to that of a light ray striking a polished glass surface. The obvious difference is that light can be both transmitted *and* reflected from the surface while a classical particle is transmitted *or* reflected. The rule for transmitting a particle across the interface is simply that if it can be transmitted it will be, otherwise it will be reflected. More precisely, if

$$|\cos(\gamma_0)|<p_1/p_0, \tag{13}$$

the particle is transmitted with the angle γ_1 given by Eq. (12). In analogy with total internal reflection in optics, $\gamma_1=\pi/2$ leads to

$$|\cos(\gamma_0)|=p_1/p_0. \tag{14}$$

The solutions of Eq. (14), denoted by $\gamma_{\rm cr}^+$ and $\gamma_{\rm cr}^-$, are centered on $\gamma=\pi/2$. Particles incident within

$$\gamma_{\rm cr}^-<\gamma<\gamma_{\rm cr}^+ \tag{15}$$

cross the billiard boundary.

A particle not transmitted across the boundary must stay in the region it came from. Since the parallel component of momentum is still conserved, Eq. (12) still holds with $p_0=p_1$, yielding

$$\cos\ \gamma_0=\cos\ \gamma_1. \tag{16}$$

This embodies the law for specular reflection, which in our coordinate system must be taken to be $\gamma_1=-\gamma_0$, that is, reflection by the same angle with respect to the tangent. This is the only possibility for the bound problem, namely, $E<0$.

Applying these rules to scattering billiards leads to the following results. A particle incident from the outside (asymptotic region) will always be transmitted to the inside (interaction region). On the outside we have $p_0=\sqrt{2E}$ while on the inside $p_1=\sqrt{2E+2}$ so

$$p_1/p_0=\sqrt{1+1/E}>1>|\cos\ \gamma_0|\forall E>0. \tag{17}$$

On the other hand, for a particle incident from the inside

$$p_1/p_0=\sqrt{E/(E+1)}=|\cos(\gamma_{\rm cr}^{\pm})|<1\forall E>0. \tag{18}$$

So the particle may be transmitted $[|\cos(\gamma_0)|\leqslant\sqrt{E/(E+1)}]$ or reflected $[|\cos(\gamma_0)|>\sqrt{E/(E+1)}]$. Equation (18) shows that there is always a critical angle for reflection no matter how energetic the particle is.

From the scattering perspective we are only interested in trajectories that will intersect the shape function. These interesting scattering initial conditions will be in one-to-one correspondence to points in the bound map. However, when a scattering trajectory is exiting the interaction region the map point will have a negative γ value between 0 and $-\pi$. The γ value is always positive for the bound map and the scattering map until escape. We transform the exit domain into the region between the $\gamma_{\rm cr}$ lines (see Fig. 8) by using the positive γ of the bound particle with the same incident angle. The entire domain of the scattering map therefore becomes the same as that of the bound map; this is crucial in understanding the connection between these two maps. The domain for both maps is $0\leqslant\gamma\leqslant\pi$ and $-\pi<\theta\leqslant\pi$. The phase space of the scattering map is partitioned into the asymptotic region between $\gamma_{\rm cr}^-$ and $\gamma_{\rm cr}^+$ and the interaction or bound region, which makes up the rest of the phase space. Thus the first and last bounce of scattering trajectory are always in the range $\gamma_{\rm cr}^-<\gamma<\gamma_{\rm cr}^+$.

III. BOUND MAP AND PHASE SPACE

The bound and scattering maps share the same phase space; it follows that the scattering problem is influenced by the same structures in phase space as that of the bound map. With this in mind we first study the bound problem.

A. Periodic orbits and symmetry lines

Knowledge of the periodic orbits is key to understanding the phase space of the map. Several orbits and their map coordinates can be guessed quite easily; for instance, the period two ($P2$) orbits, one along the x axis and the other along the y axis. While the existence of others may be obvious, their coordinates are not easy to find; like the period three ($P3$) and four ($P4$) orbits. There are still others whose mere existence may not be as obvious, i.e., those generated via bifurcations of the above mentioned orbits.

An elegant construct for finding periodic orbits in ''reversible'' maps involves the use of *symmetry lines* [13–16]. These follow from the fundamental symmetries of the problem, in our case time reversal invariance and geometrical symmetries of $r_s(\theta)$. This leads to three distinct symmetry operations for our map: momentum reversal ($\mathbf{R}_p$), reflection about the x axis ($\mathbf{R}_x$), and reflection about the y axis ($\mathbf{R}_y$). They are defined by

$$\mathbf{R}_p\begin{pmatrix}\theta\\ p\end{pmatrix}=\begin{pmatrix}\theta\\ -p\end{pmatrix}, \tag{19}$$

$$\mathbf{R}_x\begin{pmatrix}\theta\\ p\end{pmatrix}=\begin{pmatrix}-\theta\\ p\end{pmatrix}, \tag{20}$$

$$\mathbf{R}_y\begin{pmatrix}\theta\\ p\end{pmatrix}=\begin{pmatrix}\mathrm{sgn}(\theta)\pi-\theta\\ p\end{pmatrix}, \tag{21}$$

with

$$\mathrm{sgn}(\theta)\equiv\begin{cases}1, & \theta\geqslant 0\\ -1, & \theta<0.\end{cases}$$

The operators $\mathbf{R}_p,\mathbf{R}_x,\mathbf{R}_y$ are clearly their own inverses. Each also inverts the map,

$$\mathbf{M}^{-1}=\mathbf{TMT}, \tag{22}$$

where $\mathbf{T}$ represents any one of the three operators, $\mathbf{R}_p,\mathbf{R}_x$, or $\mathbf{R}_y$.

All reversible area preserving maps can be factored into a product of two *orientation reversing involutions* or symmetry operators [13],

$$\mathbf{M}=\mathbf{I}_1\mathbf{I}_0. \tag{23}$$

We are interested in the three factorizations of the map given by

$$\mathbf{M}=\mathbf{I}_1\mathbf{I}_0=\{\mathbf{MT}\}\mathbf{T}. \tag{24}$$

So

$$\mathbf{I}_0=\mathbf{T}, \tag{25}$$

TABLE I. The symmetry lines Γ_0 and Γ_1 and their branches for the symmetries $\mathbf{R}_x$, $\mathbf{R}_y$, and $\mathbf{R}_p$. The second subscript refers to the different solutions or branches of Eq. (28).

Symmetry line	Equation	Domain
$\Gamma^x_{0,0}$	$\theta(p)=0$	$\forall p$
$\Gamma^x_{0,1}$	$\theta(p)=\pi$	$\forall p$
$\Gamma^y_{0,0}$	$\theta(p)=-\pi/2$	$\forall p$
$\Gamma^y_{0,1}$	$\theta(p)=\pi/2$	$\forall p$
Γ^p_0	$p(\theta)=0$	$\forall \theta$
$\Gamma^x_{1,0}$	$p(\theta)=\dfrac{r_s'(\theta)\sin(\theta)+r_s(\theta)\cos(\theta)}{\sqrt{r_s^2(\theta)+r_s'^2(\theta)}}$	$\theta\geqslant 0$
$\Gamma^x_{1,1}$	$p(\theta)=-\dfrac{r_s'(\theta)\sin(\theta)+r_s(\theta)\cos(\theta)}{\sqrt{r_s^2(\theta)+r_s'^2(\theta)}}$	$\theta<0$
$\Gamma^y_{1,0}$	$p(\theta)=\dfrac{r_s'(\theta)\cos(\theta)-r_s(\theta)\sin(\theta)}{\sqrt{r_s^2(\theta)+r_s'^2(\theta)}}$	$0\leqslant\lvert\theta\rvert<\dfrac{\pi}{2}$
$\Gamma^y_{1,1}$	$p(\theta)=-\dfrac{r_s'(\theta)\cos(\theta)-r_s(\theta)\sin(\theta)}{\sqrt{r_s^2(\theta)+r_s'^2(\theta)}}$	$\dfrac{\pi}{2}\leqslant\lvert\theta\rvert<\pi$
Γ^p_1	—	—

$$\mathbf{I}_1=\mathbf{MT}. \tag{26}$$

The above operators represent the first two in an infinite hierarchy of symmetries defined by

$$\mathbf{I}_n=\mathbf{M}^n\mathbf{I}_0, \quad n=0,1,\ldots, \tag{27}$$

where $\mathbf{M}^n$ represents n compositions of $\mathbf{M}$.

To utilize this infinite hierarchy of symmetries we need to determine the invariant sets or *symmetry lines* associated with each of the involutions, I_n. The symmetry lines are the solutions of

$$\Gamma_n:\{\xi|\mathbf{I}_n\xi=\xi\}, \tag{28}$$

where $\xi\equiv(\theta,p)$ is a point in the map. The symmetry lines satisfy the following recursion relation [14]

$$\mathbf{M}^m\Gamma_n=\Gamma_{2m+n}. \tag{29}$$

Letting $n=0$ will generate all of the *even* symmetry lines:

$$\mathbf{M}^m\Gamma_0=\Gamma_{2m}.$$

Letting $n=1$ will generate all of the *odd* symmetry lines:

$$\mathbf{M}^m\Gamma_1=\Gamma_{2m+1}.$$

We will call the lines Γ_0 and Γ_1 the *fundamental symmetry lines* of the map. The fundamental symmetry lines for each of the possible involution pairs can be calculated analytically and are presented in Table I.

Note that there are two branches for each of the spatial symmetry lines while there is only one branch for the Γ^p_0 symmetry line and no solution for Γ^p_1. The immediate result of the nonexistent Γ^p_1 is that there are no odd symmetry lines for momentum reversal. It follows that there are no momentum reversal symmetric odd period orbits.

A periodic orbit is defined by

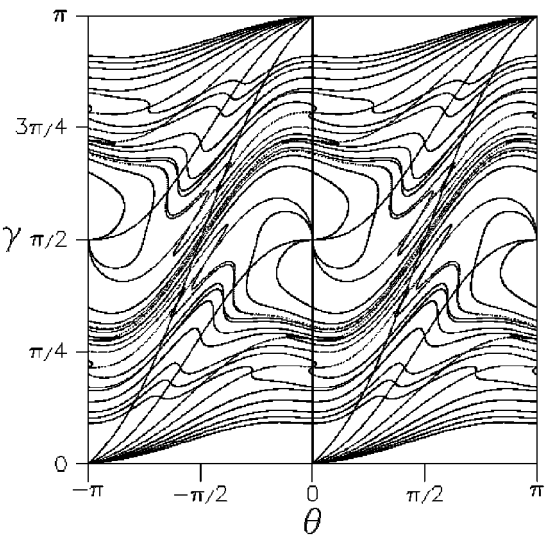

FIG. 2. Both branches of the ten symmetry lines from Γ^x_0 to Γ^x_9 for $b=0.15$. All angles are in radians in this and subsequent figures unless otherwise noted.

$$P_n:\{\xi|M^n\xi=\xi\}, \tag{30}$$

that is, the n period points are invariant under n applications of the map. This set includes orbits whose periods are divisors of n as well. The important result from the symmetry line theory [15,13] is

$$\Gamma_n\cap\Gamma_m\subset P_{n-m}. \tag{31}$$

Using this method the search for symmetric periodic orbits reduces to finding the intersections between different symmetry lines.

Figure 2 shows the symmetry lines from Γ^x_0 to Γ^x_9 for the deformation, $b=0.15$. Each of these lines has two branches; the two vertical lines at $\theta=0$ and $\theta=\pi$ are $\Gamma^x_{0,0}$ and $\Gamma^x_{0,1}$ and the two branches 0 and 1 of Γ^x_1 to Γ^x_9 start at $(0,\pi)$ and (π,π), respectively. Periodic orbits can be obtained from the intersections of these symmetry lines. As an example Fig. 3 shows the intersection $\Gamma^x_0\cap\Gamma^x_9$ (we drop the x superscript label from here on).

The periodic orbits $P3$ and $P9$ are located at the intersections of these two lines. The orbits are labeled by their winding numbers, which is determined by counting the number of times, k, the symmetry lines have ''wrapped around'' the cylinder defined by θ beginning with the smallest γ. We will come back to the fact that the orbits labeled 6/9 and 3/9 consist of three intersections each. The winding number of the orbits obtained from $\Gamma_{n,j}\cap\Gamma_{m,i}$ is formally given by

$$\omega=\begin{cases}\dfrac{2|k_m-k_n|}{|m-n|}, & i=j\\[2ex] \dfrac{2|k_m-k_n|+1}{|m-n|}, & i\neq j,\end{cases} \tag{32}$$

with $k_m=0,\ldots,|m|-1,\ k_n=0,\ldots,|n|-1,$

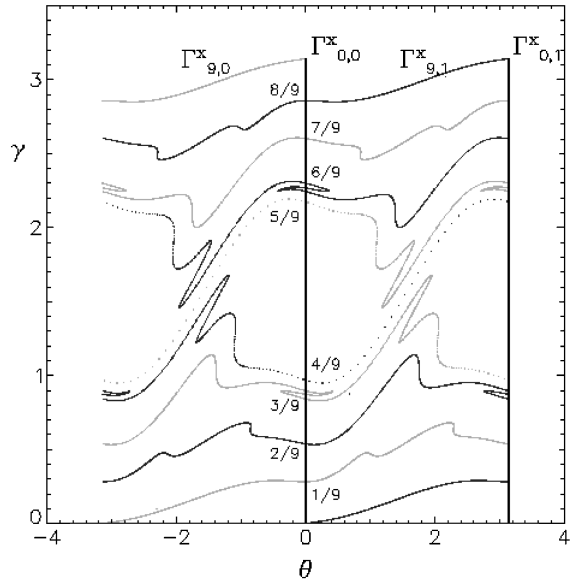

FIG. 3. The symmetry lines $\Gamma^x_{0,0}$, $\Gamma^x_{0,1}$, $\Gamma^x_{9,0}$, and $\Gamma^x_{9,1}$ for $b=0.15$. The orbits found along $\theta=0$ are labeled by their winding numbers.

where k_m (k_n) is the number of times the $\Gamma_{m,i}$ ($\Gamma_{n,j}$) symmetry line has wrapped around the cylinder. As shown in Fig. 3 the $\Gamma_{0,0}\cap\Gamma_{9,0}$ and $\Gamma_{0,0}\cap\Gamma_{9,1}$ gives us all of the $P9$ orbits that have a vertex at $\theta=0$ and reflection symmetry about the x axis. All of the $P9$ orbits labeled in Fig. 3 are shown in Fig. 4. The $\Gamma_{0,1}\cap\Gamma_{9,0}$ and $\Gamma_{0,1}\cap\Gamma_{9,1}$ give all of the $P9$ orbits that have a vertex at $\theta=\pi$ and reflection symmetry about the x axis.

B. Bifurcations

Bifurcation diagrams summarize the behavior of dynamical systems as parameters are varied; they describe how periodic orbits are created, destroyed, or collide. The symmetry lines can be used to obtain bifurcation information. In Fig. 4 there are three orbits labeled with winding number 6/9 (and three with 3/9). The local twisting of the Γ_9 symmetry line indicates that a bifurcation of some kind has occurred at some smaller b value. In Fig. 4 the sequence of orbits on the right shows the three orbits resulting from this twist of the symmetry line. The ordering is as shown: the 2/3 orbit is between the two $P9$ orbits labeled 6/9+ and 6/9−. It is instructive to examine this segment of the symmetry lines as a function of b to gain a better understanding of the nature of this bifurcation.

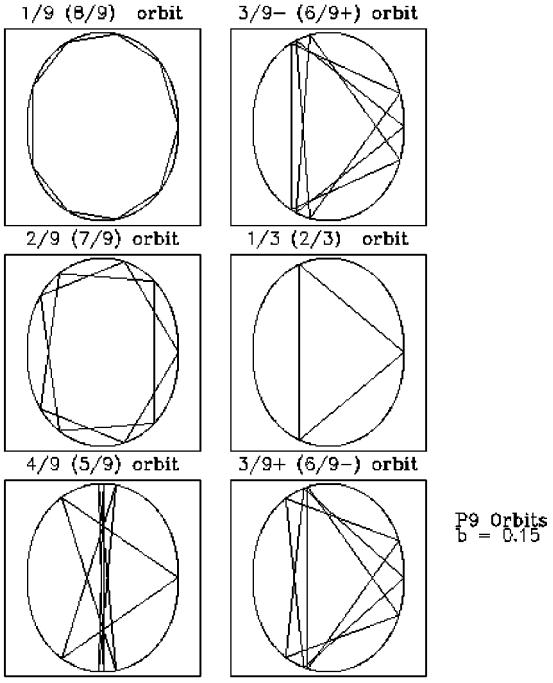

FIG. 4. The $P9$ orbits resulting from Fig. 3.

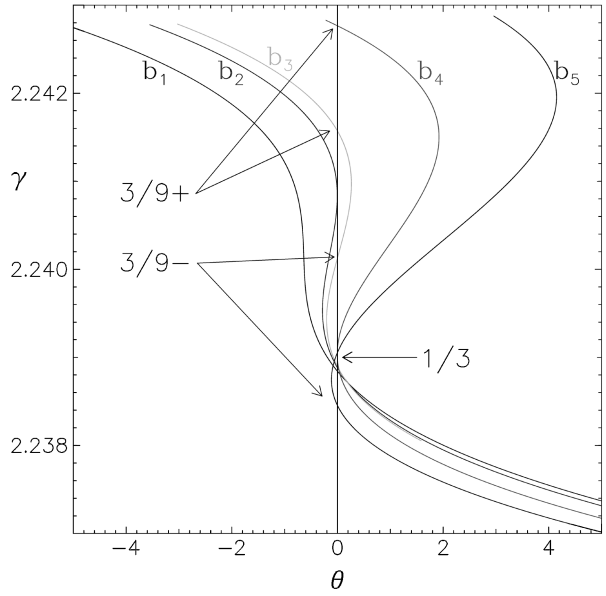

FIG. 5. A blowup of $\Gamma_9\cap\Gamma_0$ around the ''6/9'' intersections showing deformation parameters from before the bifurcation to after the bifurcation. The values of the deformations b_i are quoted in the text. θ has units of 10^{-4} rad.

Figure 5 shows a blow up series of the $\Gamma_{9,0}\cap\Gamma_{0,0}$ for different values of b ranging from before to after the bifurcation. This series reveals that before the bifurcation there is only the 2/3 orbit (e.g., $b_1=0.12175$). At $b=b_2=0.121\,787$ there is a saddle center bifurcation that creates stable (6/9+) and unstable (6/9−) $P9$ orbits. After this bifurcation the two $P9$'s are next to each other and the $P3$ is below them (e.g., $b_3=0.1218$) until the unstable $P9$ collides with the $P3$ orbit at $b=b_4=0.12187$ and they pass through each other, resulting in the situation pictured in Fig. 4. Figure 6 shows the phase space around one of the $P9$ fixed points (a) after the tangent bifurcation but before the collision ($b=b_3$) and (b) after the collision ($b=b_5=0.12195$). This type of bifurcation is referred to by MacKay [13,17] as an ''m bifurcation'' and is a generic bifurcation of area preserving maps. The bifurcation diagram for this bifurcation is shown in Fig. 7. The original orbit is labeled by its winding number, 6/9. Two $P9$ orbits are created in a saddle center and the unstable one passes through the original period 6/9 orbit. The two steps to this bifurcation are the saddle center creation of two orbits followed by the collision of one of these with the generating orbit. These two steps occur at different values of $p=\cos(\gamma)$; in general, they may occur at the same value of p, $\Delta p=0$. All of the generic bifurcations

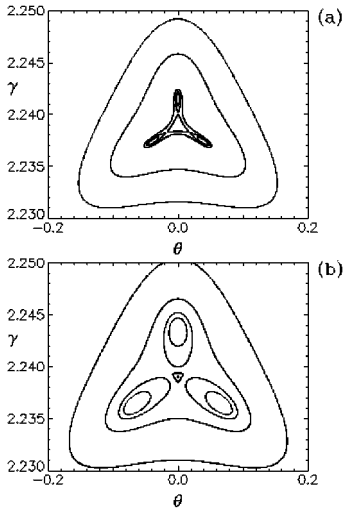

FIG. 6. Phase space near one of the $P3$ fixed points (a) for $b=0.1218$ and (b) $b=0.12195$.

of area preserving maps are discussed in several references [13,18–20,17].

C. The $P2$ and $P4$ orbits

The current investigation is primarily focused on a billiard with a deformation of $b=0.15$. At $b=0$ the billiard is circular and the phase space consists of periodic orbits with rational winding numbers (resonant tori) and quasiperiodic orbits with irrational winding number (irrational tori). As the b is increased from zero the resonant tori are all destroyed, leaving isolated periodic orbits. On the other hand, many of the irrational tori persist for $b>0$. These irrational tori stretch across the phase space, creating natural momentum boundaries. At $b=0.15$ nearly all of the original irrational tori have been broken, leaving nothing but isolated islands and chaotic orbits. So, in principle there is no dynamical partitioning of the phase space into different momentum regions as is the case with smaller deformations. Thus the phase space is expected to be quite complicated. Yet, in spite of this complexity the low period orbits play a key role in the dynamics.

Of particular importance are the $P2$ and $P4$ orbits. There are two $P2$ orbits, one stable and the other unstable. The stable orbit lies along the x axis and has the map coordinates $(0,\pi/2),(\pi,\pi/2)$; the two periodic points are surrounded by large regions filled with KAM tori. Figure 8 shows the KAM regions associated with the stable $P2$ orbit along with several other stable periodic orbits and two chaotic trajectories. Also seen in this Fig. 8 are the stable $P4$ orbits with winding number 1/4 and 3/4. Their tori are surrounded by four $P8$ orbits created during an ''m bifurcation'' of the $P4$ orbits. In configuration space the stable $P4$ is diamond shaped with vertices at $\theta=0,\ \pm\pi/2$, and π.

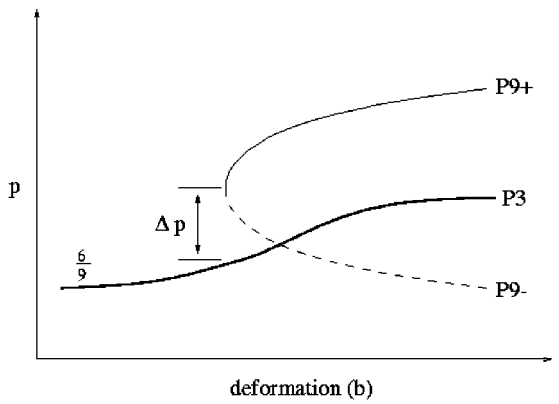

FIG. 7. The bifurcation diagram for the ''m bifurcation'' associated with the 2/3 orbit.

The unstable counterparts of the $P2$ and $P4$ orbits mentioned above are equally important. The unstable $P2$ orbit lies along the y axis and has the map coordinates $(\pi/2,\pi/2)$, $(-\pi/2,\pi/2)$. The unstable $P4$ orbits trace out a rectangle in configuration space, with the long sides parallel to the y axis. The 1/4 orbit follows this path in a counterclockwise direction while the 3/4 orbit follows the same path in a clockwise direction. Unstable orbits are characterized by their stable and unstable manifolds. Figure 9 shows approximations to the stable manifolds of the unstable $P2$ orbit and the $P4$ orbit with winding number 3/4. A manifold is an invariant set under the mapping (or inverse mapping); in other words, a point on a manifold maps to a point on a manifold. Iterating a suitable subset of points belonging to the manifold will generate an approximation to the whole manifold. The simplest (approximate) subset of the manifold can be obtained by linearizing the map around a periodic point. The linearized map provides the ''stability matrix,'' which, for simple closed billiards, has a general analytical solution given by Berry [3]. The stability matrix can be diagonalized to find the stable (negative eigenvalue's eigenvector) and unstable (positive eigenvalue's eigenvector) directions at the periodic points. To generate the stable manifolds shown in Fig. 9 we begin with a large (10^5) set of initial conditions from a small segment (10^{-8}) of a line lying along the stable direction and centered on a periodic point. These initial conditions are then iterated under the inverse map, $\mathbf{M}^{-1}$, for about 30 iterates. Beyond ~ 30 iterations small deviations of the initial set of points from the actual manifold start to become large, producing large deviations from the actual manifold.

The $P2$ and $P4$ orbits' manifolds and KAM regions occupy a large portion of the map and so are important in understanding the dynamics. However, there are an infinite number of other periodic orbits that play a role in the dynamics. The ones that are particularly important for the analysis in the next section are periodic orbits whose stable islands have bifurcated away, leaving nothing but unstable periodic points and their manifolds. A particular set of such orbits that we will examine more closely are those with winding numbers between 1/2 and 3/4. The manifolds of these orbits are sandwiched between and intimately intertwined with the $P2$ and $P4$ manifolds of Fig. 9. In the next section we will relate the gross scattering properties to the $P2$ orbits and the finer scale structure of the scattering to the low period unstable orbits near the asymptotic region of the scattering phase space.

IV. SCATTERING

A scattering experiment consists of launching positive energy particles from an asymptotic region towards an interaction region and observing their ''states'' upon leaving the

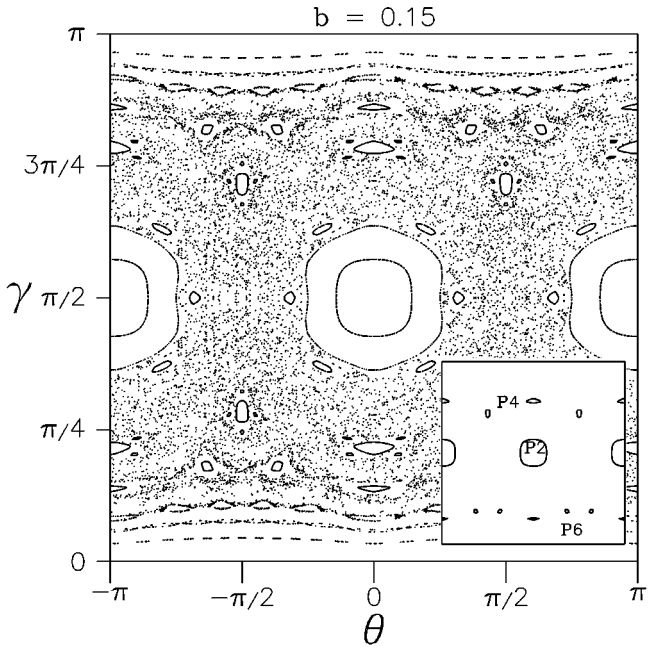

FIG. 8. The map featuring some of the remaining KAM regions around the stable $P2$, $P4$, and $P6$ orbits as well as some higher period orbits. Also shown are two $P6$ island chains around the $P2$ and two chaotic trajectories. The inset is to help the reader identify the periodic orbits.

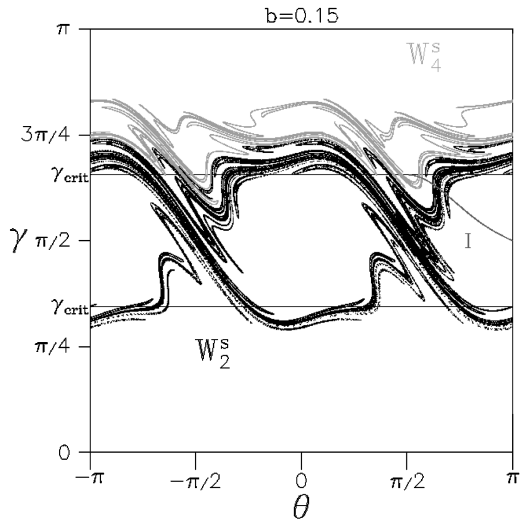

FIG. 9. The stable manifolds of the 1/2 orbit and the 3/4 orbit along with the $\gamma_{\rm cr}^{\pm}$ lines for $E=0.2856$. Also shown is the set of initial conditions, I, corresponding to $y_0 \geqslant 0$, $p_{y0}=0$, and $p_{x0}=+\sqrt{2E}$.

interaction region. For the billiard problem the asymptotic region is the area outside the billiard and the interaction region is the area inside and including the billiard boundary. The ''state'' observed on leaving the interaction is often the escape angle, Φ, that a trajectory makes to an arbitrary fixed axis. Another interesting quantity to observe is the ''delay time,'' which is defined as the amount of time a particle remains in the interaction region.

In terms of the bound billiard map the asymptotic region is defined by the area between the critical angles, $\gamma_{\rm cr}^{\pm}$. The interaction region is the area above $\gamma_{\rm cr}^{+}$ and below $\gamma_{\rm cr}^{-}$. Figures 8 and 9 each show the bound phase space with the critical angle lines $\gamma_{\rm cr}^{\pm}$ separating the asymptotic from the interaction region. A scattering trajectory will have exactly two map points in the asymptotic region (between $\gamma_{\rm cr}^{\pm}$); one corresponding to its entry into the billiard and the other corresponding to its exit. In general a scattering trajectory may also have an arbitrary number of points in the interaction region of the map corresponding to being trapped in the potential region. The number of map points, n, that a trajectory has in the interaction region corresponds to the number of times it hits the billiard wall without escaping (bounces); this is effectively equivalent to the delay time. Thus the scattering map looks just like the bound map with horizontal lines corresponding to the critical angles dividing the phase space into asymptotic and interaction regions.

In scattering problems one typically defines an impact parameter that is a simple function of initial conditions. For two-dimensional nonintegrable dynamical systems a general analysis requires that the space of impact parameters also be two dimensional. However, as we will demonstrate below, a well chosen one-dimensional impact parameter is sufficient to characterize the chaotic nature of our billiard scattering system. For our analysis we launch particles from a line at fixed x_0 outside the well and parallel to the y axis with fixed momentum components $p_{x0}=\sqrt{2E}$, and $p_{y0}=0$. The impact parameter is y_0. We will record the scattering functions Φ and n as functions of y_0. The angle Φ is measured with respect to the $+x$ axis. Figure 10 shows a series of enlargements of the scattering function $\Phi(y_0)$ for $b=0.15$. The

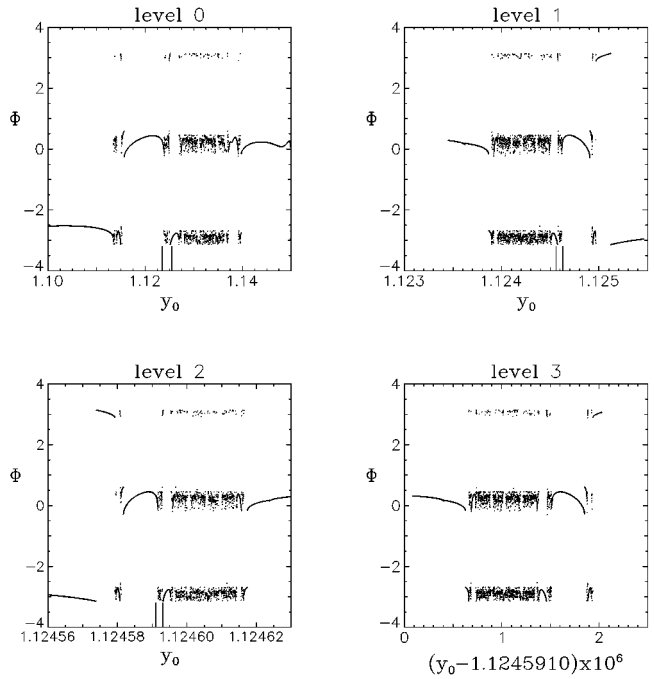

FIG. 10. A series of enlargements of escape angle vs impact parameter for $E=0.2856$ and $b=0.15$. The large hash marks on the y_0 axis indicate the region enlarged in the next level. The trajectories are all launched from the left of the potential region with $p_y=0$ and $p_x=\sqrt{2E}$. The deformation here is $b=0.15$ and the energy is $E=0.2856$. The escape angle is the angle of the momentum vector measured from the $+x$ axis.

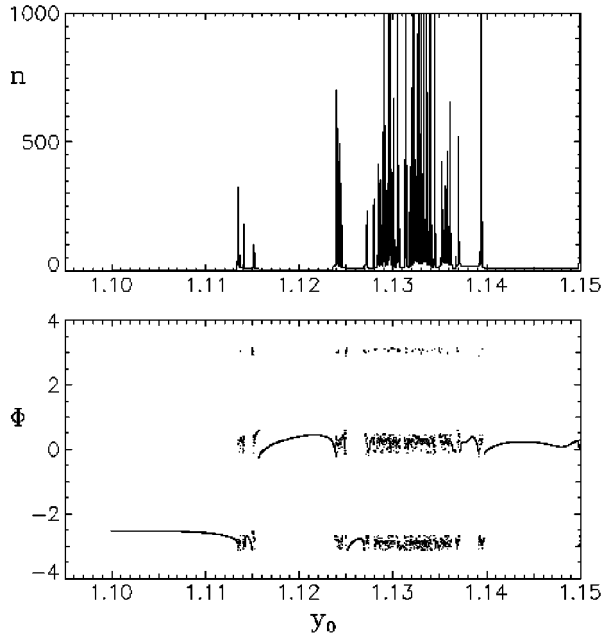

FIG. 11. Top: the number of bounces, n, before escaping vs the impact parameter, y_0. Bottom: the escape angle Φ as a function of impact parameter.

level-0 plot excludes the relatively uninteresting range of impact parameters $0<y_0<1.1$ where trajectories bounce only one, two, or three times before escaping. Note that in the range of impact parameters shown all trajectories bounce four or more times before escaping. There are several interesting features of these plots. First, there are clearly regions where the scattering is regular, i.e., piecewise continuous, separated by ''unresolved'' regions. Second, the ''odd'' enlargements (e.g., levels 1 and 3) are mirror images of the ''even'' enlargements. Third, the scattering is predominately in the forward and backward directions while other angles are clearly excluded, indicating preferred scattering directions. Fourth, the figures show a striking self-similarity that persists on all scales attainable with double-precision floating point arithmetic. We will address each of these points in turn and then ask whether such features persist when we allow all possible scattering initial conditions.

The behavior of the scattering function of Fig. 10 is the hallmark of a chaotic scattering system [21–24]. The smooth regions are sets of initial conditions that bounce the same number of times before exiting. They are separated by regions where the escape angle appears unresolved or ''chaotic'' as a function of impact parameter. As Fig. 10 shows this behavior persists to higher magnification of an unresolved region so that at any magnification there are always chaotic regions in the escape angle function. Figure 11 shows (top) the number of bounces, n, before escaping versus the impact parameter and (bottom) the escape angle versus impact parameter (this is Fig. 10, level 0). This shows that the chaotic regions are related to trajectories that bounce a large number of times before escaping. The more bounces a particle undergoes the more sensitive the outgoing angle is to small displacements in the impact parameter. The singularities in the function $n(y_0)$ form an uncountable infinity of points; the impact parameters that lead to infinite n form a fractal set.

The origin of this fractal set lies in the stable manifolds of the homoclinic orbits of the system. The manifolds themselves are of measure zero in phase space so that a typical initial condition will not fall exactly on a manifold. However, initial conditions that find themselves near one of these manifolds will tend to move toward the periodic orbit before moving away. If the periodic orbit is entirely in the interaction region then the particle may be trapped for an arbitrarily long time as it approaches the periodic orbit. For chaotic scattering to occur these manifolds must reach into the asymptotic region where the initial conditions live. For billiard systems the asymptotic region is defined by the critical angles for escape. Thus there can be chaotic scattering only if the stable manifolds of periodic orbits that live in the interaction region cross the critical angle.

A. $P2$ and $P4$ manifolds

Figure 9 shows an approximation to the stable manifolds of the $P2$ orbit and one of the $P4$ orbits along with the critical angle lines defining the asymptotic region. We also show the line of initial conditions, I, that produced the results in Figs. 10 and 11. The $P4$ manifold lays on the $P2$ manifold and mixes with it at their ''interface.'' In between the $P4$ and $P2$ manifolds there are an infinite number of other unstable periodic orbits whose stable counterpart periodic orbits have bifurcated at smaller deformations and whose stable manifolds are intimately intertwined with the $P2$ and $P4$ manifolds. As we will see below, these orbits are responsible for the structure of the scattering functions, in particular, the scaling and relative sizes of smooth regions seen in the scattering functions.

Scattering trajectories that are initialized near the stable manifolds of periodic orbits living in the asymptotic region will have very short scattering times. For example, the unstable $P2$ orbit is such an orbit. Its stable manifold dominates the asymptotic region so that most initial conditions will find themselves close to it; the resulting trajectories will bounce only a few times, if they bounce at all, before escaping. Scattering trajectories that are initialized near the stable manifolds of periodic orbits that live in the interaction region will exhibit long scattering times. The $P4$ orbit is an example of this type; its stable manifold reaches the asymptotic region where scattering trajectories may come close to it.

B. Preferred scattering directions

The presence of the large KAM zones around the stable $P2$ orbit restricts the manifolds (and therefore, the chaotic trajectories) to the two ''neck'' regions around $\theta=\pm\pi/2$. It is ultimately a result of the existence of large $P2$ KAM zones in the phase space that restricts particles to exit in either one of these neck regions. The extent of the $P2$ manifolds limits the momentum range of the escaping particles. Thus the $P2$ orbits are the source of the bidirectional nature of the scattering functions. In this section we present a way to get a more quantitative measure of the degree of directionality found in the escape angle function.

The preferred directions apparent in Fig. 10 are independent of the particular choice of scattering initial conditions. That is, the same preferred directions and range of escape angles result from nearly any line of initial conditions that

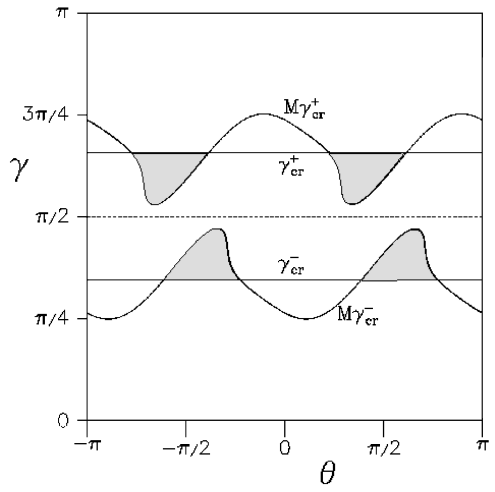

FIG. 12. The critical angle lines and their images under one iteration of the map for $b=0.15$ and $E=0.2856$. The shaded regions represent areas through which particles that have bounced at least once will exit.

we choose. To show this consider a set of initial conditions consisting of the two lines γ_{cr}^{+} and γ_{cr}^{-} under one forward iteration of the map. Iterating the boundary between the asymptotic and interaction regions in this way we obtain an image of the boundary one bounce later. Since the mapping is orientation preserving the phase space above γ_{cr}^{+} maps to the phase space above $\mathbf{M}\gamma_{cr}^{+}$ and below γ_{cr}^{-} maps to below $\mathbf{M}\gamma_{cr}^{-}$. Figure 12 clearly shows there are well-defined areas of the asymptotic region into which trapped particles must go. The allowed regions of escape for particles that have bounced at least once are defined by the four shaded lobes in Fig. 12. It also shows that at this energy ($E=0.2856$) and deformation ($b=0.15$) particles that are trapped in the upper phase space (clockwise rotating orbits) will never reach the lower phase space (counterclockwise rotating orbits).

The areas defined by the shaded lobes of Fig. 12 are easily converted into escape angle ranges. The plot shown in Fig. 13 shows these escape angle ranges overlaid on the billiard shape for initial conditions above γ_{cr}^{+}, that is, clockwise rotating orbits. We find that the escape angle must fall within the two limits given by

$$-1.0709<\Phi<0.9355,$$

$$-4.2125<\Phi<-2.0609. \tag{33}$$

These limits apply to all initial conditions starting anywhere in the upper interaction region. The range of escape angles observed in Fig. 10 certainly falls within these bounds. Later we will address the fact that the escape angle ranges observed in Fig. 10 are much smaller than the ones given in Eq. (33). Thus, we have an upper bound on the range of escape angles for any set of initial conditions in the upper interaction region. The ranges can be reflected about $\Phi=0$ to obtain the range for initial conditions in the lower interaction region.

We can verify the existence of the preferred directions as well as add distribution information by launching a large set of initial conditions evenly distributed in the asymptotic region. We consider 10^6 initial conditions in the rectangle given by $-\pi<\theta<\pi$ and $\pi/2<\gamma<\gamma_{cr}^{+}=2.061\,596$ (corresponding to $E=0.2856$) keeping track of the number of bounces before exiting. Figure 14 shows a histogram of the number of trajectories, N, binned according to (a) escape angle Φ and (b) the θ value at escape, Θ. This figure shows trajectories that have bounced four or more times (there are no three or five bounce trajectories). Here we see that the range of escape angles Φ is precisely what is observed in Fig. 10. Had we included ''fly-by,'' one bounce, and two bounce trajectories in the histogram the directionality would still be apparent. However, the range of escape angles would be wider. If we continue the process of excluding the fewest bounces further we will find the distribution and range remains essentially unchanged. This rapid convergence with the number of bounces implies that it takes about four

FIG. 13. The escape angle ranges obtained from the shaded lobes of Fig. 12 overlaid on the billiard shape for initial conditions above γ_{cr}^{+}.

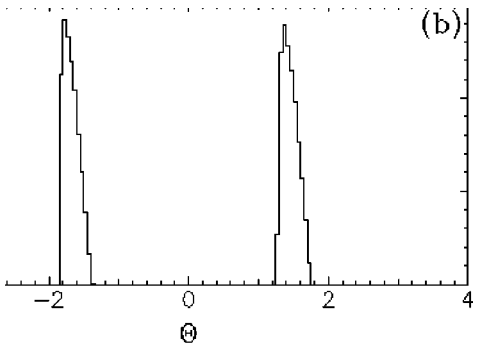

FIG. 14. The number of trajectories N binned by (a) escape angle Φ and (b) exit angle Θ including all trajectories with more than three bounces. The data are from 10^6 initial conditions launched between $-\pi<\theta<\pi$ and $\pi/2<\gamma<2.061596$ corresponding to $E=0.2856$ and a deformation parameter of $b=0.15$.

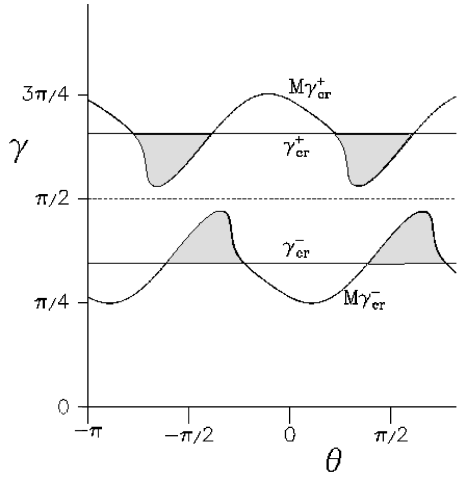

FIG. 15. The critical angle lines and their images under one iteration of the **inverse** map for $b=0.15$ and $E=0.2856$. The shaded regions represent areas that lead to trajectories that bounce at least once.

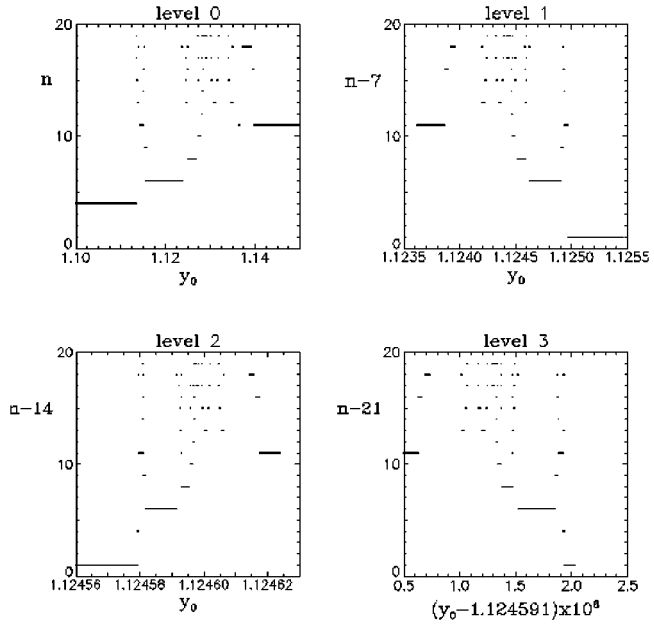

FIG. 16. Number of bounces n before escaping as a function of impact parameter y_0. This series covers the same impact parameter regions as Fig. 10. The n axis is offset by seven and truncated to a range of $\Delta n=20$ at each enlargement to illuminate the role of the $P7$ orbit and enhance the self-similarity between enlargement levels.

bounces for a chaotic scattering trajectory to ''forget'' where it came from. This is so since the distribution of outcomes of all possible initial conditions is well reproduced by a small sample of initial conditions. Of course the small sample of initial conditions cannot be completely arbitrary; it must pass through a ''relevant'' region of phase space. What precisely constitutes the relevant region is the subject of the next paragraph.

C. Chaotic region

We can invert the question answered by Fig. 12 and ask: ''What part of the asymptotic region leads to trajectories that bounce at least once?'' To answer this we take the critical angle lines and iterate them once with the inverse map to get Fig. 15. Trajectories beginning in the shaded lobes will enter the interaction region for at least one bounce. Consider this picture overlaid on Fig. 9. A large portion the shaded region of Fig. 15 is occupied by the stable manifold of the $P2$ orbit. This portion of the shaded regions will lead to nearly all of the one and two bounce orbits. The manifolds that lie between the $P2$ and $P4$ are responsible for the longer orbits. Most important are unstable periodic orbits whose periodic points lie entirely in the interaction region but whose manifolds reach into the asymptotic region. These are responsible for the structure of the scattering functions.

To illuminate this connection we look at the escape time functions associated with the series of enlargements of Fig. 10. These are shown in Fig. 16. We choose to enlarge the chaotic regions between the two largest smooth regions inside a chaotic band; thus we are looking at the largest scale feature of the scattering functions. Clearly one level can be scaled into another. We have already identified the n scale by offsetting each enlargement by seven. In Fig. 17 we have plotted the trajectories associated with the impact parameter at the center of the largest smooth regions in each level, i.e., $n=6$ of level 0 in Fig. 16. We see that these trajectories all start near the 5/7 orbit (shown in Fig. 18) and follow it around one more time for each enlargement. This implies that the period seven orbit should have a periodic point very close to the asymptotic boundary and, since the trajectory can bounce at all seven vertices, all of its periodic points lie in the interaction region. This is verified in Fig. 19, which shows an approximation to the 5/7 manifold, the circles represent the periodic points of the orbit.

The $P7$ orbit is also responsible for the length scaling between levels in Fig. 16 by way of its stable manifold. In

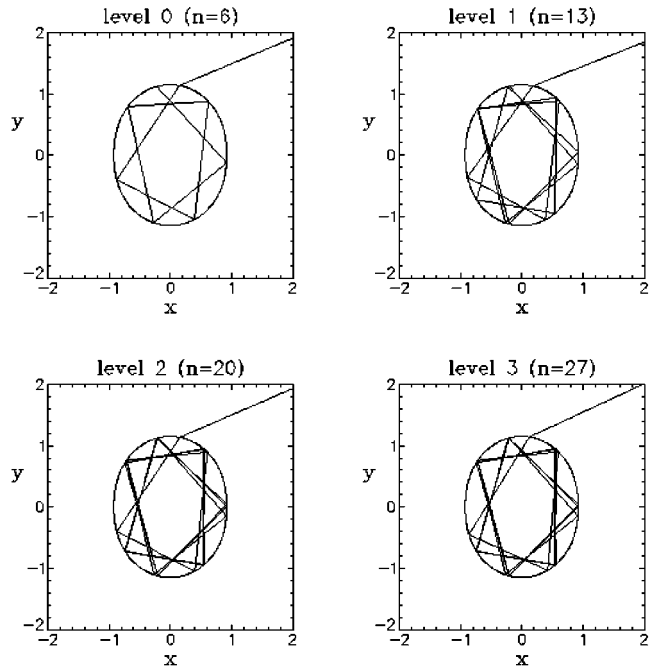

FIG. 17. The shortest orbits in each of the levels of Fig. 16. The trajectories are chosen from the center of the largest smooth regions in each level.

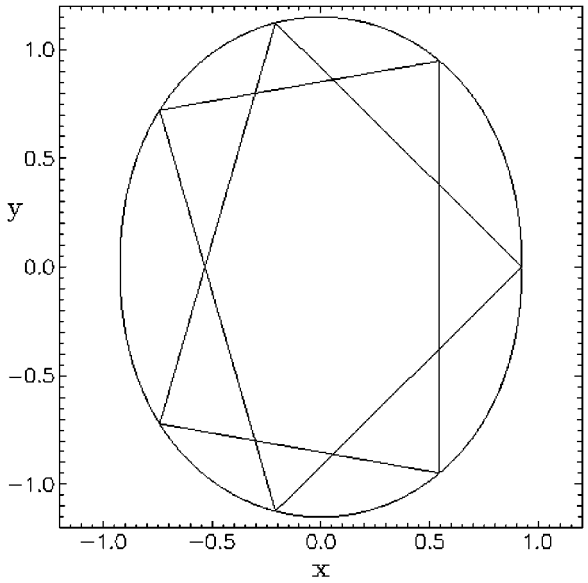

FIG. 18. The 5/7 orbit that is approached by the orbits in Fig. 17.

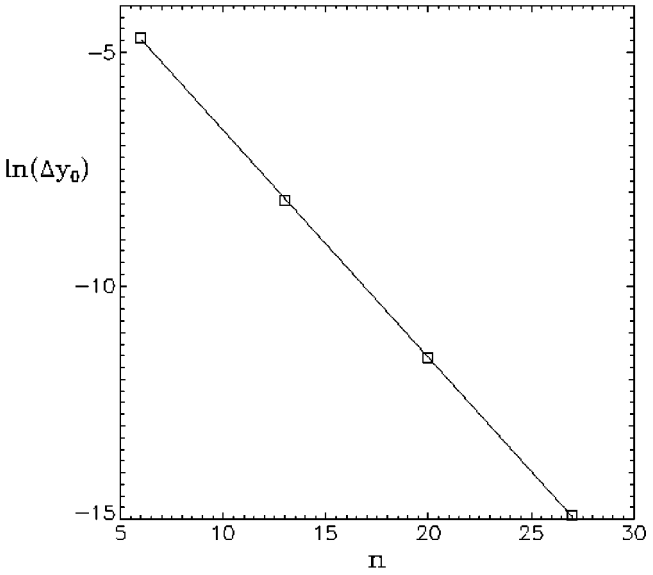

FIG. 20. A plot of $\ln(\Delta y_0)$ vs n with the Δy_0's are the lengths of the longest region in each of the levels of Fig. 16. Also shown is a linear fit to this data giving a slope of $m=-0.4867$.

Fig. 20 we plot the natural log of the length of the longest regions in each plot, $\ln(\Delta y_0)$, versus the number of bounces to escape, n. The points are well fit by a straight line with a slope of $m=-0.4867$. Since the set of initial conditions is transverse to the 5/7 manifold the scaling relationship in the scattering functions is a direct measure of the scaling of distances between ''fingers'' of the 5/7 manifold. This suggests that the scale factor found above may be related to the Lyapunov exponent of the 5/7 orbit. The Lyapunov exponent is found to be $\lambda \approx 0.42$. The details of this relationship will be investigated elsewhere. Figure 21 shows a sketch of the stable manifold W_s, periodic point marked P, the line of initial conditions I, and the γ_{cr}^{+} line. Note that we have represented the spacing between intersections of I and W_s as approximately constant when, as we have just seen, the spacing should decrease exponentially as the periodic point is approached.

Figure 21 also provides an explanation for the reflection symmetry between the adjacent levels of Fig. 16. For instance, to scale level 1 into level 2 we must reverse the orientation of the impact parameter as well as scale the lengths. This orientation reversing arises from the fact that the initial conditions for adjacent levels fall on alternating sides of the stable manifold. We see that the line of initial conditions associated with each level alternates from one side of the manifold to the other. In terms of the manifold sketched in Fig. 21 mapping the finger labeled ''0'' into the finger labeled ''1'' requires reflecting I about their common point and rescaling. We must also reflect about the line of initial conditions and scale, however, this transformation

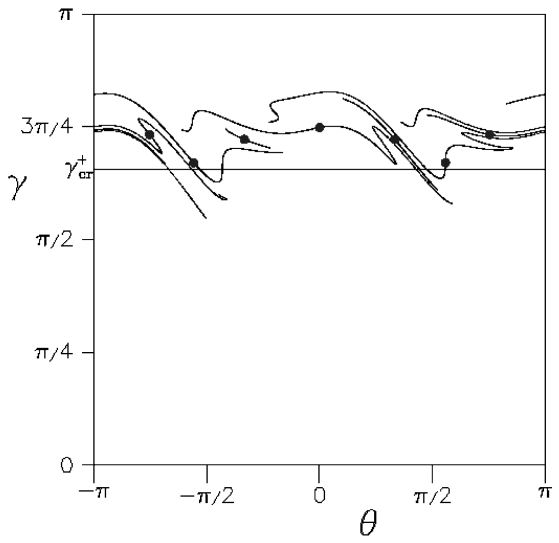

FIG. 19. An approximation to the 5/7 manifold. The periodic points are indicated by the black dots.

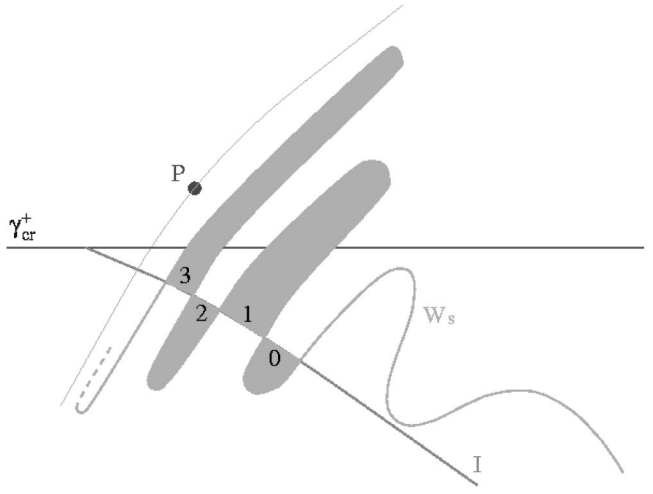

FIG. 21. A sketch of the stable manifold near a periodic point in the interaction region (above γ_{cr}^{+}). The line labeled I represents initial conditions. The numbers correspond to the level of enlargement of scattering functions.

TABLE II. The lowest period orbits up to $P19$ with winding numbers between 2/3 and 3/4. The bottom row of numbers orders them from lowest to highest period. The $P4$ is effectively a boundary orbit and is labeled by ∞, indicating it as the source of the finest scale structure.

$\frac{2}{3}$	$\frac{11}{16}$	$\frac{9}{13}$	$\frac{7}{10}$	$\frac{12}{17}$	$\frac{5}{7}$	$\frac{13}{18}$	$\frac{8}{11}$	$\frac{11}{15}$	$\frac{14}{19}$	$\frac{3}{4}$
		↑	↑	↑	↑	↑	↑	↑	↑	↑
		4	2	6	1	7	3	5	8	∞

cannot affect the one-dimensional scattering functions.

Now that we understand the mechanism that produces the largest scale features of the scattering functions, below we examine the next largest features. To this end we looked at a set of pictures similar to those of Fig. 16 where the enlargements are taken from the leftmost chaotic region in the level 0 plot ($1.116 \lesssim y_0 \lesssim 1.118$). This series of enlargements looks identical to Fig. 16, except for the range of impact parameters involved. Here, however, we find that the largest smooth regions in each level are 10 bounces apart. The orbit responsible for the scaling in this series is the 7/10 orbit. The length scales by 0.45 between levels while the Lyapunov exponent of the 7/10 orbit is $\lambda \approx 0.400$. The same reasoning that we used for the 5/7 orbit applies here; the characteristics of the unstable 7/10 manifold are responsible for the self-similar nature of these structures.

The process of identifying prominent smooth regions and their adjacent chaotic regions with certain periodic orbits can be continued. The next orbit found in this way is the 8/11. The pattern that emerges from this process is that the largest features are controlled by the lowest period orbits left in the interaction region. For the range of energies for which the 3/4 orbit is still in the interaction region this orbit behaves approximately like a boundary orbit; the very finest features (longest escape time trajectories) of the scattering function show orbits converging to the 3/4 orbit. This is only approximately true since there are higher winding number orbits whose manifolds find their way past the 3/4 and reach the asymptotic region. The property of the $P4$ orbit that distinguishes it as a boundary orbit is the fact that the stable $P4$ orbit has not yet been destroyed by bifurcations while all of the other orbits between the $P2$ and $P4$ are unstable. The $P4$ KAM tori that remain force the flux of trajectories into channels containing the unstable orbits that slow the momentum diffusion of the trajectory.

Using the approximation that the 3/4 orbit presents a phase space boundary we can develop an algorithm to predict the sequence of orbits responsible for the successively smaller features of the scattering function. Consider all periodic orbits whose winding numbers are between the 3/4 orbit and the next lower period orbit that falls in the asymptotic region, in the current example this is the 2/3 orbit. The orbits are ordered from the lowest winding number to the highest up to some desired periodicity. If an orbit has a periodic point in the asymptotic region, then all orbits of lower winding number are also in the asymptotic region and are excluded. The remaining orbits are then ordered from the lowest period (largest structures) to the highest (smaller structures), excluding the boundary orbit 3/4. The sequence for $E = 0.2856$ is shown in Table II for orbits up to $P19$. The location of the cutoff winding number (indicated by the vertical bar in Table II) for a fixed deformation is a function of energy. We see that as the energy is increased, orbits are removed from the sequence and the scaling properties of the scattering function change.

V. CONCLUSIONS

We have studied chaotic scattering on a quadrupole deformed billiard. The results obtained have general applicability despite our use of a specific billiard geometry. We showed the existence of preferred chaotic scattering directions. We have explained the origin and organization of the self-similar structure of the scattering functions in terms of unstable periodic orbits of the bound billiard system. Periodic orbits of the bound system were found using symmetry line theory and the stable manifolds of some of the unstable orbits were calculated.

We have shown that the existence of preferred scattering directions is independent of the choice of initial conditions. This is true provided the chosen set of initial conditions intersect the stable manifolds of periodic orbits in the interaction region. The escaping trajectories are restricted to leaving the billiard domain in the regions of sharpest curvature. This ''localization'' of the chaotic scattering trajectories results from the existence and persistence of large $P2$ KAM regions in the bound phase space. This forces trajectories to be funneled into the two regions between the tori, which correspond to the large curvature regions of the billiard. The trajectories are also localized in escape angle. This is a consequence of the degree of stretching of the phase space enforced by the $P2$ manifolds. Increasing the deformations will increase the stretching of the phase space, making the allowed escape angle range larger (for a fixed energy). The only requirement for the $P2$ orbits to play such a central role is that the billiard wall be concave everywhere. The details of the functional form of the shape are not important as long as integrable billiard geometries (circle, ellipse) are avoided.

The nearly perfect self-similar structure of the scattering functions is a result of the fractal structure of the stable manifolds of periodic orbits in the interaction region. Each such orbit contributes to the structure and scaling of the scattering functions. The most influential orbits, in the sense that they are associated with the scaling of the chaotic regions separated by the largest smooth regions, are the lowest period orbits that are still in the interaction region at the chosen scattering energy. Since the interaction region is defined by the particle energy, changing the energy will change the scattering functions. However, for small changes in energy for which the lower period orbits remain in the interaction region the large scale structure should remain roughly unchanged. Only when the lowest period orbits fall in the asymptotic region will there be a major structural change in the scattering functions.

We presented a general algorithm for relating the periodic orbits to the self-similarity of scattering functions. There are, however, several caveats that apply to this simplistic picture. First, we have assumed that the Birkoff orbits, those that arose from the undeformed circular billiard, are the only contributors to the structure of the scattering functions. This view omits effects due to other orbits such as bifurcations of

the Birkoff orbits. For the large scale structure that we have examined the omission seems justified but we expect that the existence of these orbits should have some noticeable effect on smaller scales. The other caveat concerns our ability to sort out the relative sizes of smooth and chaotic regions. Beyond the three regions that we have examined and attributed to the lowest three periodic orbits it is difficult to determine where to look next. Nevertheless, the algorithm still sheds some light on the origins of the structure of the scattering functions. With these considerations in mind the algorithm will also be applicable to higher-energy scattering where the $P4$ orbit is in the asymptotic region. The 3/4 orbit then becomes the lower boundary in the same sense that the 1/2 orbit is a lower boundary in specific example discussed. The upper boundary will be the next higher period orbit with KAM tori remaining. For the deformation used throughout this paper ($b=0.15$) that orbit is the 5/6.

We also provided a systematic means of finding the symmetric periodic orbits of the bound billiard by way of symmetry lines. As long as $r_s(\theta)$ retains the two spatial symmetries $\mathbf{R}_x$ and $\mathbf{R}_y$ the six fundamental symmetry lines given in Table I are generally applicable. From these symmetry lines and the application of the map the infinite hierarchy of symmetry lines can, in principle, be found. The intersections of these lines provide the location in phase space of the periodic points of all the symmetric periodic orbits. The symmetry line methodology is extremely powerful and can be automated to make the determination of periodic orbits particularly easy. This becomes an important consideration when semiclassical methods such as trace formulas are being applied. This is an important direction of future research since many of the interesting physical systems that can be modeled by billiards are mesoscopic systems lying on the border between the quantum and classical worlds.

There are other interesting situations that we have left unaddressed. If the particle energy is lowered significantly the corresponding asymptotic region shrinks and eventually the upper (lower) lobes of Fig. 12 will overlap the lower (upper) interaction region. This should represent a significant change in the scattering dynamics in the sense that some trajectories escaping the upper (lower) interaction region will be reinjected into the lower (upper). The effect will be to increase the lifetime of some trajectories without introducing an infinitely self-similar structure since they will still be primarily near the $P2$ manifold and therefore attracted to the asymptotic region. To put this another way, the signal will be a lot noisier. However, the directionality of the scattering will be just as pronounced since the KAM islands of the $P2$ will still be in effect and the escape angle will necessarily be close to $\pi/2$.

Finally, changing the deformation parameter, particularly making it smaller, will substantially change the bound phase space and therefore the scattering. If there are irrational tori remaining they will impose natural boundaries to the momentum diffusion of trajectories. This should generally produce a simplification in the self-similar patterns of the scattering functions since there will be an absolute winding number barrier beyond which the asymptotic region is inaccessible.

ACKNOWLEDGMENTS

This work was partially supported by a grant from the National Science Foundation. We would like to thank Charles Jaffe for his insightful discussions.

[1] L. Bunimovich, Funct. Anal. Appl. **8**, 254 (1974).
[2] L. Bunimovich, Commun. Math. Phys. **65**, 259 (1979).
[3] M. V. Berry, Eur. J. Phys. **2**, 91 (1981).
[4] Y. G. Sinai, Russ. Math. Surv. **25**, 137 (1970).
[5] M. Robnik, J. Phys. A **16**, 3971 (1983).
[6] C. Regie Brown, Edward Ott, and Celso Grebogi, Phys. Rev. Lett. **59**, 1173 (1987).
[7] O. Bohigas, D. Boosé, R. Egydio de Carvalho, and V. Marvulle, Nucl. Phys. A **560**, 197 (1993).
[8] R. Jenus, U. Nöckel, and Douglas Stone, Opt. Lett. **19**, 1693 (1994).
[9] Reinhold Blümel, T. M. Antonsen, Jr., B. Georgeot, Edward Ott, and R. E. Prange, Phys. Rev. E **53**, 3284 (1996).
[10] W. Bauer and G. F. Bertsch, Phys. Rev. Lett. **65**, 2213 (1990).
[11] Harold U. Baranger, Rodolfo A. Jalabert, and A. Douglas Stone, Chaos **3**, 665 (1993).
[12] Jenus U. Nöckel and Douglas Stone, Nature (London) **385**, 45 (1997).
[13] R. S. MacKay, Ph.D. thesis, Princeton University, 1982.
[14] L. E. Piña, Physica D **26**, 369 (1986).
[15] J. Heagy, Ph.D. thesis, Drexel University, Philadelphia, 1989.
[16] J. F. Heagy and J. M. Yuan, Phys. Rev. A **41**, 571 (1990).
[17] J. M. Mao and J. B. Delos, Phys. Rev. A **45**, 1746 (1992).
[18] M. Baranger and K. T. R. Davies, Ann. Phys. (N.Y.) **177**, 330 (1987).
[19] M. Baranger, K. T. R. Davies, and J. H. Mahoney, Ann. Phys. (N.Y.) **186**, 95 (1988).
[20] Alfredo M. Ozorio de Almeida, *Hamiltonian Systems: Chaos and Quantization* (Cambridge University Press, Cambridge, 1988).
[21] Bruno Eckhardt and Christof Jung, J. Phys. A **19**, L829 (1986).
[22] C. Jung and H. J. Scholz, J. Phys. A **20**, 3607 (1987).
[23] S. Bleher, E. Ott, and C. Grebogi, Phys. Rev. Lett. **63**, 919 (1989).
[24] V. J. Daniels, M. Vallières, and J. M. Yuan, Chaos **3**, 475 (1993).